Dark Signal Quantization and Random Telegraph Signal in a Quanta Image Sensor

Joanna Krynski[1,2], Daniel McGrath[2], Alexandre Le Roch[1], Sarah Holloway[2], Lucrezia Migliorin[2],
Vivian Bernard[1],Valérian Lalucaa[1], Alex Materne[1], Cédric Virmontois[1], Vincent Goiffon[2]
1. CNES, 18 Av. Edouard Belin, 31400 Toulouse, France,
2. ISAE-SUPAERO, Université de Toulouse, 10 av. Marc Pélegrin, 31055 Toulouse, France.
E-mail: joanna.krynski@cnes.fr, Phone: +33 07 44 88 91 53

I. INTRODUCTION

Single-photon detection is a requirement for many scientific, defense and commercial applications [1]–[3]. The principle of photon counting relies on accurately resolving the number of single photoelectrons generated in the photosensitive area. The task of resolving such a low signal can be difficult due to parasitic noise such as thermal shot noise and electronic readout sources. Commercial CMOS-based devices called quanta image sensors (QIS) possess such low levels of dark current that, in combination with their deep sub-electron circuit read noise, enables single-photon counting [4]. Characterizing the noise of detectors is an integral part of determining their viability for certain applications. In this work, the dark current characteristics of a Gigajot QIS16 camera are investigated [5]. The sensor uses $45\,\mathrm{nm}/65\,\mathrm{nm}$ backside illuminated CIS process, with $1.1\,\mu\mathrm{m}$ pitch pixels in a 4096 x 4096 array. In addition to the high conversion gain and low dark current, the camera uses correlated multiple sampling (CMS) during readout to reduce further noise contributions [5].

In this study, we use dark signal histograms to accurately discriminate the sensor's offset, noise and mean dark current at a single electron resolution. With the extremely low noise levels of this sensor it is possible to observe spatial and temporal dark current quantization. We also study noisy pixels and find evidence of original dark current and MOSFET random telegraph signal (RTS) behaviors. Pixels with MOSFET RTS exhibit dark signal histograms with multiple, equally-distributed peaks which we attribute to the CMS operation. We support this claim with CMS simulation results.

II. DARK SIGNAL QUANTIZATION

In a QIS, the histogram of pixel values from a single dark frame, here called the Dark carrier Counting Histogram (DCH) (Fig. 1), can provide the mean conversion gain, the number of dark charges per pixel, the mean dark current, the digital offset, and the noise. This is similar to the Photon Counting Histogram technique of QIS characterization [6]–[9], but in the absence of illumination.

The discrete peaks of the DCH demonstrate the dark carrier population is quantized spatially, a result which was previously seen in a much smaller region-of-interest (ROI) by Ma et al. [8]. We find that the resolution of the quantized peaks does not vary with the size of the ROI, demonstrating a very good uniformity of pixel response.

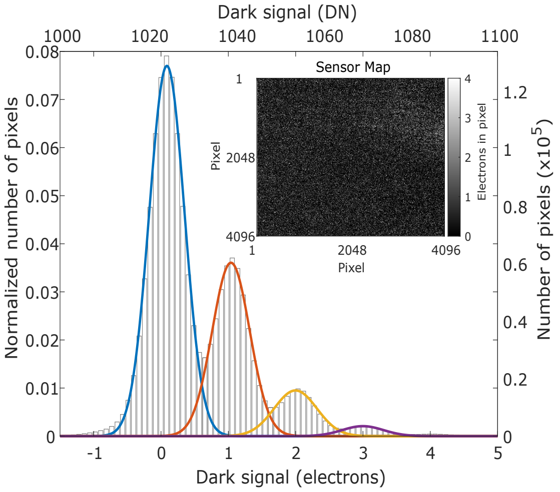

Fig. 1: A histogram of the signal from a single full sensor (16.7 Mpixels) dark frame (inset) at $35\,^{\circ}\mathrm{C}$, with $8\,\mathrm{s}$ integration time. Each peak is fit with a Gaussian curve which permits to extract the mean dark signal in the pixel and the spatial noise.

A DCH constructed from thousands of acquisitions of the same pixel provides evidence of temporal quantization of dark carrier generation (Fig. 2). As each peak represents the number of electrons in the pixel per integration time, the thermal electron generation rate can be extracted, and the dark current density can be estimated. By repeating the data acquisition at several temperatures, we observe the temperature-dependence of dark carrier generation on a pixel-by-pixel basis. The resulting DCHs (Fig. 2) exhibit the expected shift of the mean to higher dark signal values as the the mean thermal electron generation rate increases with temperature.

The log of the mean dark current of the pixel against inverse temperature is plotted to highlight a linear dependence (inset of Fig. 2). This demonstration of the Arrhenius law can be used to estimate the activation energy of the dark current source of this particular pixel. The temperature dependence of the dark current follows the square of the intrinsic carrier concentration, n_i^2, with an apparent activation energy around $1.1\,\mathrm{eV}$. This provides evidence that the source of this pixel's dark current is not dominated by Shockley-Read-Hall

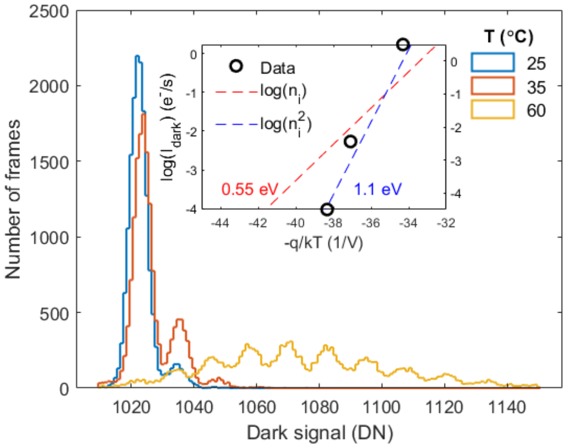

Fig. 2: DCH of single pixel depicted in at three temperatures for 2 s integration time. The histogram is constructed by reading the pixel dark signal over 16,000 times. The inset shows the mean dark current plotted in a log scale against inverse temperature to extract the dark current activation energy.

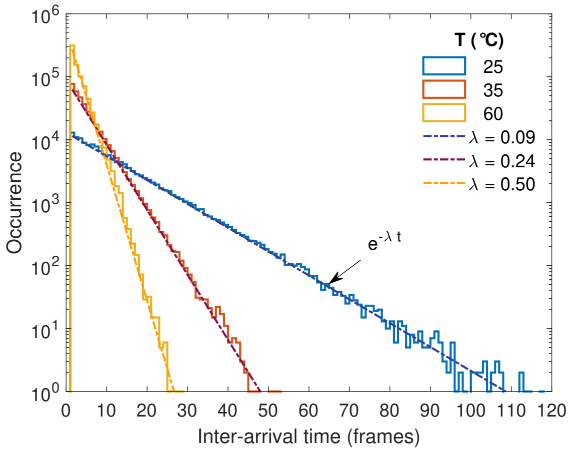

Fig. 3: Dark electron inter-arrival time distribution in a single pixel over long-term acquisition at several temperatures. The dashed curves represent an exponential fit to the distribution.

generation from mid-gap states, which would exhibit a temperature dependence similar to n_i (i.e. activation energy around $0.55\,\mathrm{eV}$) [10].

With the ultra-low ($\sim 0.29\ \mathrm{e}^-_{\mathrm{rms}}$) noise of the QIS, it is possible to probe the nature of dark current generation. Figure 3 shows the distribution of the time between dark electron emissions at several temperatures. The time between dark electron generation events appears to be exponentially distributed, which is an experimental confirmation that dark electron generation is a Poisson process [11]. The distribution is parametrized by one value, λ - the mean number of events per unit time. Multiplying by the integration time directly gives the dark current I_{dark}, while the dark carrier lifetime in the pixel can then be computed through $\tau_{\mathrm{dark}} = 1/I_{\mathrm{dark}}$. This result has previously been experimentally elusive, since legacy electron-counting technologies exhibited much higher dark currents such that the generation rate was generally

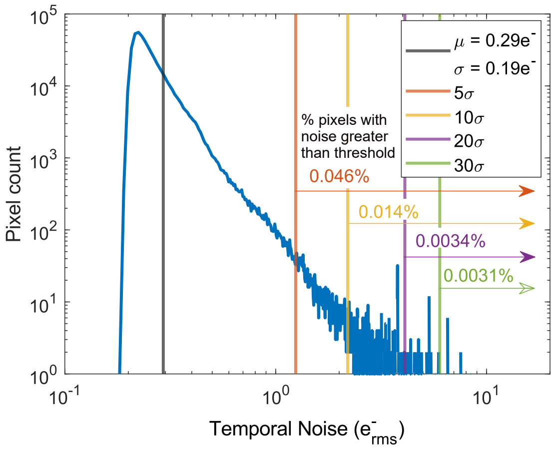

Fig. 4: Temporal noise distribution for studied sensor area of 500 kpixels. The gray vertical line is the mean of the distribution (μ), while colored lines show the distance from the mean in factors of the distribution's standard deviation (σ). The percentage of pixels with noise values greater than these thresholds is indicated above the arrow.

continuous rather than discrete.

III. RANDOM TELEGRAPH SIGNAL

The improvements to the CIS process have driven down the pixel dark currents to historic lows such that the majority of the pixels in this QIS retain nearly no dark charges at short integration times. We study the noise characteristics of a 512 x 1023 region of the Gigajot camera by taking 5000 dark frames with $1\,\mathrm{ms}$ integration time at a fixed temperature of $35\,^{\circ}\mathrm{C}$. Temporal noise is calculated as the standard deviation of the pixel dark signal over the total number of frames. The resulting histogram (Fig. 4) shows that most pixels have very low noise, with a mean of 3.5 DN (equal to $0.29\ \mathrm{e}^-_{\mathrm{rms}}$, with the nominal conversion gain of $12\ \mathrm{DN}/\mathrm{e}^-$) and spread (standard deviation) of 2.88 DN. The pixels residing in the peak of the distribution are like those of Fig. 5 (a), where there is nearly no dark charge present throughout the multi-thousand frame measurement. However, it is interesting to investigate the dark signals of the pixels residing in the tail of the distribution. We classify the noisiest pixels by their distance from the mean of the distribution.

Less than 5% of pixels are located 5 standard deviations away from the mean of the distribution in Fig. 4. Pixels at this threshold have dark signals which are uniformly spread out (Fig. 5 (c)). Above 10 standard deviations from the mean, pixel dark signal traces show discrete bands (Fig. 5 (e) and (g)). These pixels' histograms have a single prominent central peak and several small, equally spaced side peaks (Fig. 5 (f) and (h)).

In a separate measurement of a 1024x1024 region of the sensor, 45 pixels were identified to exhibit dark current-RTS, with a transition amplitude proportional to integration time, such as the pixel of Fig. 6. Some have an ON/OFF behavior with nearly $0\ \mathrm{e}^-/\mathrm{s}$ emitted in the low state and dozens of e^-/s in the high state. This represents a 0.0043% incidence of such a noise signature.

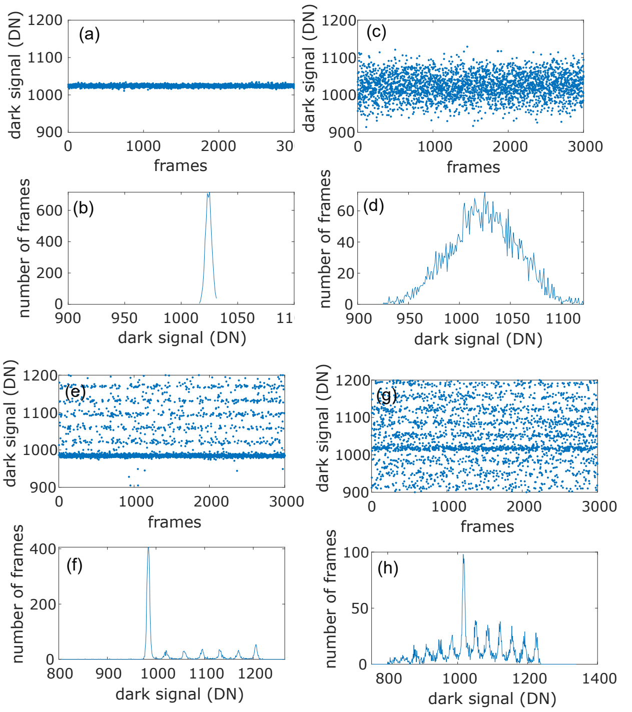

Fig. 5: Examples of observed pixel dark signal traces and their respective histograms.

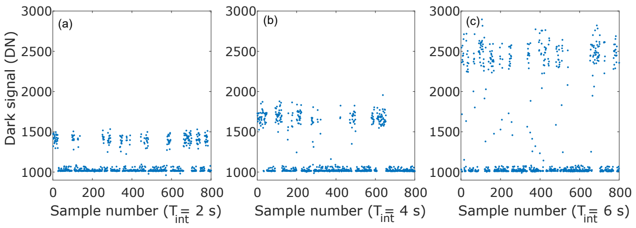

Fig. 6: Dark signal trace exhibiting a two-level RTS at various integration times.

The discrete bands of dark signal in Fig. 5 (e) and (f) are attributed to RTS induced somewhere in the readout chain (the source follower, a floating node, the column amplifier or the ADC), as they are independent of integration time. Evidence of SF-RTS is well-documented in other CIS technologies ([12]–[16]), and noted in passing by the Gigajot team [5], [17]. The appearance of discrete dark signal bands and related multi-peak DCH is present in approximately 80% of the noisiest pixels. We observe that there are always six peaks present to the side of the central peak, although there can be a strong asymmetry (Fig. 5 (f)). Generally, the separation between peaks is very uniform (∼18 DN) but varies from pixel to pixel.

There are two mechanisms which could lead to the observed dark signal noise: (1) the existence of multiple traps in the same SF, or (2) correlated multiple sampling (CMS), which differs from double sampling (CDS) in that several samples are averaged during the reference and signal sampling phases (Fig. 7). The first proposed mechanism is considered by Chao et al. [13], where up to 7-peaks are observed in a pixel with CDS. The effects of multiple sampling on the output voltage of the sampling stage are discussed in Chao et al. [15], with a hypothetical 5 sample CMS output histogram demonstrating several peaks, but experimental data was not conclusive.

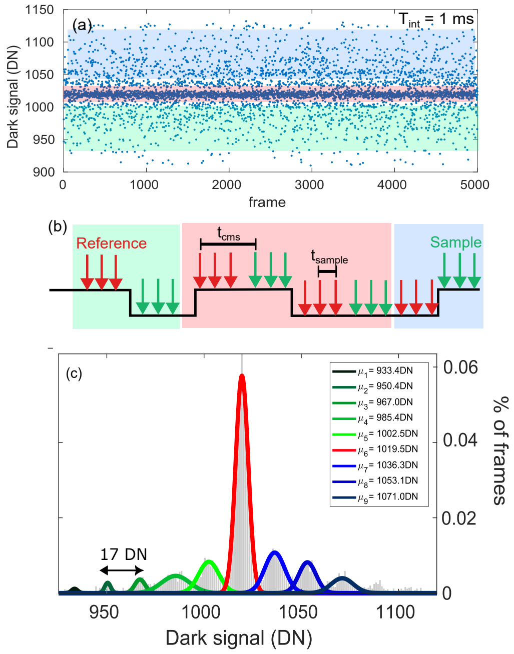

Fig. 7: (a) Dark signal of pixel; (b) RTS trace schematic with correlated multiple sampling (CMS); (c) the dark signal histogram for the same pixel. Discrete peaks arise from the combination of possible output voltages after CMS, depending on the RTS level during the two sampling phases.

IV. SIMULATION OF RTS WITH CORRELATED SAMPLING

To investigate which mechanism is more likely in the studied QIS, we simulate the output of the sampling circuit considering: (1) a pixel with multiple traps in the SF (resulting in a RTS with more than two discrete levels), followed by CDS, or (2) a two-level RTS but with CMS. The random switching of the SF voltage is determined by drawing from an exponential probability distribution parametrized by the trap emission and capture time constants, τ_e and τ_c, respectively. In the case of CDS, the simulated signal is sampled at a fixed rate of $\mathrm{t_{cds}}$. In the case of CMS, the signal is sampled m times at a rate of $\mathrm{t_{sample}} << \mathrm{t_{cms}}$ per reference and per signal phase of the CMS period. A SF MOSFET with multiple traps would exhibit multi-level RTS signals. These are implemented by generating several separate traces of varying RTS amplitudes and time constants then superimposing them.

Figure 8 shows a simulated dark signal trace before and after CDS, and the dark signal histogram of a RTS signal resulting from three traps. The side peaks are not evenly space or well-separated, and the presence of only three peaks implies that more traps would have to be present to emulate the experimentally observed six side peaks. It is possible to simulate six equally spaced peaks on each side of a large central peak, but only if the traps' amplitudes are constrained to specific multiples of each other. The possibility that a SF in a pixel of such dimensions to have three traps with the exact time constants and RTS amplitudes necessary to observe equally spaced peaks on the CDS output histogram is extremely unlikely.

By comparison, the output histogram after CMS with six samples per phase on a RTS signal resulting from

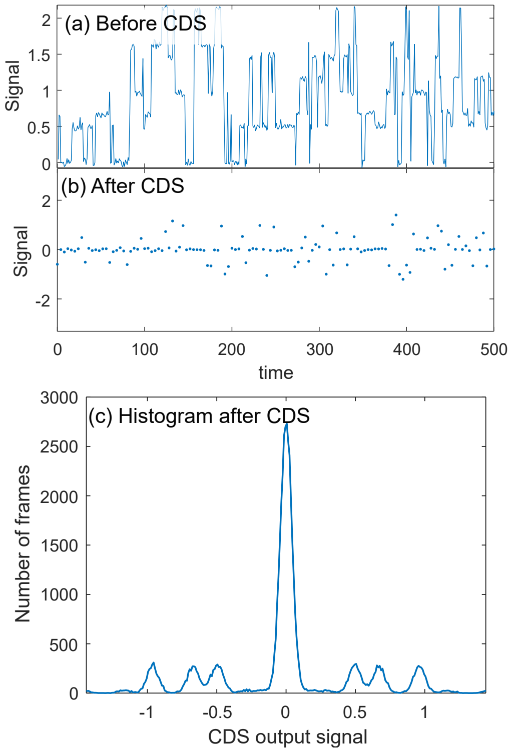

Fig. 8: Simulated dark signal resulting from superimposition of RTS signals created by 3 different traps (a) before CDS, (b) after CDS, and (c) the resulting histogram.

a single trap resembles more closely the observed experimental data (Fig. 9). 13 peaks are visible, six on each side of the center peak; the side peaks are equally spaced, and, similar to Fig. 5 (h), the peaks closest to the center are taller than those at the extremes.

The strong asymmetry observed in Fig. 5 (h) is believed to be related to the SF strong inversion condition during the CMS sampling, as discussed in [12] and [13]: due to the short inter-sampling period, there is a higher probability of the trap being occupied (i.e. low RTS level in an NMOS) during the signal sampling phase, resulting in a positive voltage after the sample subtraction. The SF inversion condition is taken into consideration in our simulation: the RTS trace in Fig. 9 (a) is probed during the reference sampling phase, while the trace in (b) is probed during the signal sampling phase.

V. CONCLUSION

In this study the dark signal of a quanta image sensor is characterized with single-electron resolution. Thanks to the ultra-low dark current and noise of this sensor, Dark carrier Counting Histograms can be used to extract several sensor metrics such as conversion gain and mean dark current. On average the pixels posses very low temporal noise but among the noisiest pixels we observe dark current and MOSFET random telegraph signal. Correlated multiple sampling appears to influence the dark signal outputs of these noisy pixels, causing discrete bands in the temporal traces and multiple, evenly spaced peaks in their histograms. Understanding and mitigating the discussed noise sources in such state-of-the-art sensors will allow for further innovation in the field of CIS photon counting technologies.

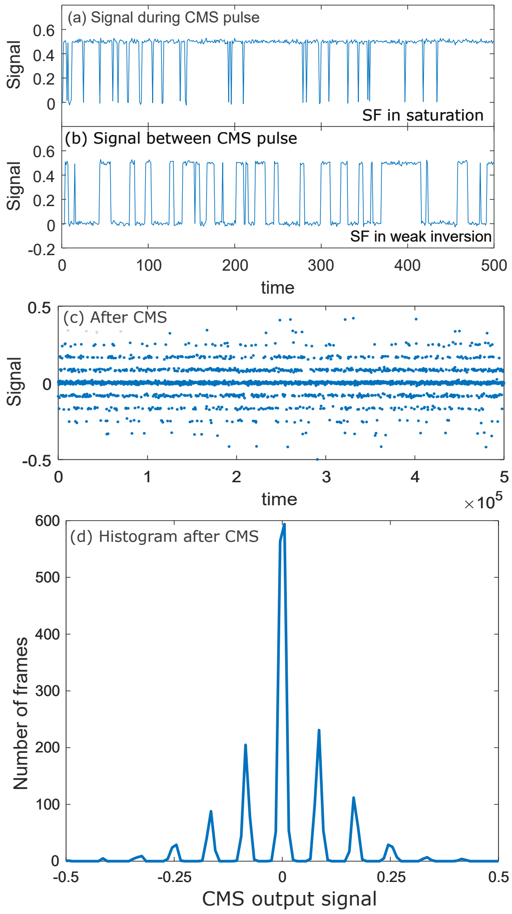

Fig. 9: Simulated two-level RTS signal (a) during the CMS pulse when the SF is in saturation and (b) between CMS pulses when the SF in weak inversion. (c) The signal after CMS, and (g) the resulting histogram.

REFERENCES

[1] J. Tiffenberg *et al.*, *Phys. Rev. Lett.*, vol. 119, no. 13, p. 131802, Sep. 2017.
[2] M. Laurenzis *et al.*, in *Proc. of SPIE*, vol. 13204. SPIE, Nov. 2024, pp. 41–51.
[3] Y. Chi *et al.*, in *Proc. of ECCV*. Cham: Springer International Publishing, 2020, pp. 122–138.
[4] E. Fossum *et al.*, *Sensors*, vol. 16, no. 8, p. 1260, Aug. 2016.
[5] J. Ma *et al.*, *IEEE Electron Device Lett.*, vol. 42, no. 6, pp. 891–894, Jun. 2021.
[6] J. Ma *et al.*, *IEEE Electron Device Lett.*, vol. 36, no. 9, pp. 926–928, Sep. 2015.
[7] D. A. Starkey *et al.*, *IEEE J. Electron Devices Soc.*, vol. 4, no. 3, pp. 129–135, May 2016.
[8] J. Ma *et al.*, *Optica*, vol. 4, no. 12, p. 1474, Dec. 2017.
[9] A. Hendrickson *et al.*, *IEEE J. Electron Devices Soc.*, vol. 11, pp. 376–384, 2023.
[10] A. S. Grove *et al.*, *Solid-State Elec.*, vol. 9, pp. 783–806, Jan. 1966.
[11] J. F. C. Kingman, *Poisson Processes*. Oxford, New York: Oxford University Press, Jan. 1993.
[12] X. Wang *et al.*, in *Proc. of IEDM*, Dec. 2006, pp. 1–4.
[13] C. Chao *et al.*, *Sensors*, vol. 17, no. 12, Nov. 2017.
[14] C. Y.-P. Chao *et al.*, *IEEE J. Electron Devices Soc.*, vol. 5, no. 1, pp. 79–89, Jan. 2017.
[15] C. Y.-P. Chao *et al.*, *IEEE J. Electron Devices Soc.*, vol. 7, pp. 227–238, 2019.
[16] C. Y.-P. Chao *et al.*, *Sensors*, vol. 19, no. 24, p. 5447, Jan. 2019.
[17] J. Ma *et al.*, *Sci Rep*, vol. 12, no. 1, p. 13869, Aug. 2022.